JACS
JOURNAL OF THE AMERICAN CHEMICAL SOCIETY

Article

pubs.acs.org/JACS

Catalytic Proton Dynamics at the Water/Solid Interface of Ceria-Supported Pt Clusters

Matteo Farnesi Camellone,[*,†] Fabio Negreiros Ribeiro,[†,∥] Lucie Szabová,[‡] Yoshitaka Tateyama,[‡] and Stefano Fabris[*,†,§]

[†]CNR-IOM DEMOCRITOS, Istituto Officina dei Materiali, Consiglio Nazionale delle Ricerche, Via Bonomea 265, 34136 Trieste, Italy

[‡]Center for Green Research on Energy and Environmental Materials (GREEN), National Institute for Materials Science (NIMS), 1-1 Namiki, Tsukuba, Ibaraki 305-0044, Japan

[§]SISSA, Scuola Internazionale Superiore di Studi Avanzati, Via Bonomea 265, 34136 Trieste, Italy

Supporting Information

ABSTRACT: Wet conditions in heterogeneous catalysis can substantially improve the rate of surface reactions by assisting the diffusion of reaction intermediates between surface reaction sites. The atomistic mechanisms underpinning this accelerated mass transfer are, however, concealed by the complexity of the dynamic water/solid interface. Here we employ ab initio molecular dynamics simulations to disclose the fast diffusion of protons and hydroxide species along the interface between water and ceria, a catalytically important, highly reducible oxide. Up to 20% of the interfacial water molecules are shown to dissociate at room temperature via proton transfer to surface O atoms, leading to partial surface hydroxylation and to a local increase of hydroxide species in the surface solvation layer. A water-mediated Grotthus-like mechanism is shown to activate the fast and long-range proton diffusion at the water/oxide interface. We demonstrate the catalytic importance of this dynamic process for water dissociation at ceria-supported Pt nanoparticles, where the solvent accelerates the spillover of ad-species between oxide and metal sites.

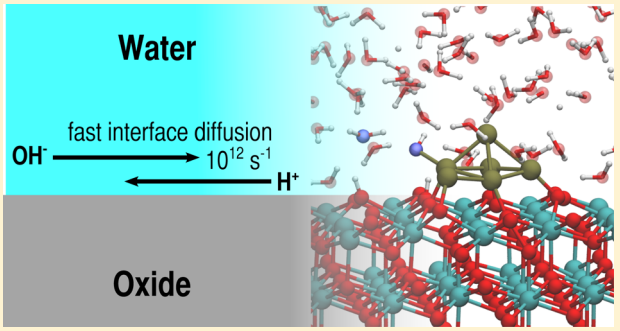

INTRODUCTION

Chemical reactions at the interface between water and solid surfaces underpin diverse fundamental biological processes and valuable technological applications including biomineralization, corrosion, photochemical water splitting, wet heterogeneous catalysis, and fuel-cell electrochemistry, to cite just a few. Water is, in fact, regularly present in ambient reaction conditions. Moreover, water-based approaches to heterogeneous catalysis in industrial chemistry are cheap and sustainable alternatives to expensive and toxic solvents.[1] In all these cases, the structure and dynamics of the first water layers in contact with the solid surface profoundly impact on heterogeneous catalysis: The effects of moisture at the active sites range from increasing the catalytic activity by orders of magnitude, as for CO oxidation on oxide-supported Au nanoparticles,[2] to deactivating the catalyst, as for methane combustion on metal−oxide catalysts.[3] These effects, resulting from the presence of interfacial water, have been shown to originate from a combination of various factors: the altered reaction mechanisms/thermodynamics and electron energy levels due to solvation,[4] the site-competition between water and reactants/intermediates,[5] or the modified mass transport between active sites.[6] Partially dissociated water molecules at the liquid/solid interface can mediate and accelerate the diffusion of H atoms on FeO films,[6−8] and can increase the proton-transfer rate on ZnO, GaN, and TiO_2 photocatalytic surfaces.[9−11] Solvent polarization effects were shown to affect the charge state of catalytic oxide-supported metal nanoparticles, to create new active sites,[12] or to affect the electron-level alignment at photocatalytic mixed-oxide photoanodes.[13] These and similar works evidenced the important and elusive effects of interfacial water molecules in wet heterogeneous catalysis and opened the question on how to control and exploit the solvent effects in catalyst design.

We show here that surface wetting strongly affects the equilibrium of water dissociation and leads to a local increase of H^+ and OH^- species at an important water/oxide catalytic interface. The increased local acidity triggers a fast Grotthus-like diffusion mechanism, which is confined in the interface region and which allows for transferring the species along the interface over several lattice sites and with diffusion rates $\sim 10^{12}$ s^{-1}. We demonstrate the catalytic importance of this effect for oxide-supported Pt nanoparticles, where this diffusion mechanism couples the water dissociation at the oxide surface sites

Received: April 8, 2016
Published: July 14, 2016

DOI: 10.1021/jacs.6b03446
J. Am. Chem. Soc. 2016, 138, 11560−11567

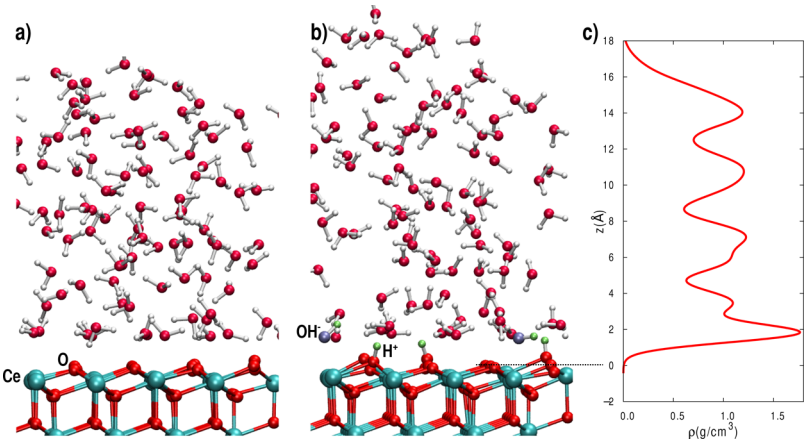

Figure 1. Snapshots from the AIMD simulations of the model interface between water and the $CeO_2(111)$ surface before (a) and after (b) partial dissociation of interfacial water. (c) Planar average profile of the water density as a function of the distance from the CeO_2 surface. The origin of the distances in the water density profile is set to the average z coordinate of the surface O atoms (see horizontal dotted line).

with the transport and adsorption of ad-species to the metal sites. The process drives electron transfer across the metal/oxide interface, affecting the nanoparticle charge, metal/support interaction, and overall chemical reactivity.

Atomic-scale imaging and spectroscopy have been applied to investigate solid/liquid interfaces[14,15] but gaining direct atomic-level insight into the chemistry of these complex interfaces remains highly challenging at real catalysis conditions of temperatures and pressures, which require going beyond standard ultra-high-vacuum (UHV) characterization tools. In addition, these interfacial effects are governed by a small number of atoms relative to the bulk phases, and their study requires experimental techniques with high interface sensitivity. In this context, ab initio molecular dynamics (AIMD) simulations have been shown to provide key atomic-level insight into interface dynamic processes of catalytic interfaces.[16] In particular, this method disclosed how the solvent alters elementary surface processes governing the catalytic properties of surface active sites, most notably the water dissociation equilibrium and dynamics at water/oxide interfaces.[17,18] While the examples studied so far focused mostly on short-range proton rearrangements, i.e., involving an interfacial water molecule and the closest surface site, the solvent can, in principle, assist also the long-range diffusion of ad-species,[8,19] which is paramount for spillover effects in catalysis, and whose mechanisms and instances are far less understood.

We address this issue by employing AIMD simulations, focusing on the solvent-induced structural and electronic effects occurring at the interface between liquid water and the surface of ceria (CeO_2). Ceria is a highly reducible oxide, which has key applications in catalysis,[20] and which promotes the effective activation and dispersion of metal nanoparticles via strong metal−oxide electronic interactions.[21−23] XPS measurements and ab initio static density functional theory (DFT) calculations at $T = 0$ K showed that water partially dissociates on the most stable $CeO_2(111)$ surface in UHV conditions.[24−29] Little is known about the atomistic structure and chemical processes of this interface in the presence of multilayer water at realistic reaction conditions, which is the subject of the present study.

■ COMPUTATIONAL METHODS

The AIMD simulations were carried out in the framework of spin-polarized density functional theory, employing the Perdew−Burke−Ernzerhof (PBE)[30] exchange-correlation functional and a Hubbard U term added to the Kohn−Sham energy functional (PBE+U). This well-established method has been shown to be a reliable approach for ceria-based systems.[10,31−33] All the calculations employed periodic boundary conditions.

The interface between the stoichiometric $CeO_2(111)$ surface and water was modeled with periodic (4×4) supercell slabs consisting of two O−Ce−O trilayer separated, in the direction perpendicular to the surface, by more than 25 Å. This space was filled with 107 H_2O molecules providing a liquid-phase thickness of about 18 Å, while an additional 7 Å of vacuum separated the water layer from the $CeO_2(111)$ periodic slab. The atoms in the lowest-laying O−Ce−O trilayer were constrained to their equilibrium bulk-like positions, while all the other atoms were free to move under the action of the interatomic forces. The results reported for this stoichiometric $CeO_2(111)$ surface in contact with water were obtained with Born−Oppenheimer AIMD performed with the CP2K code.[34] The simulations parameters were chosen following previous studies on ceria surfaces.[10,35] The core electrons were described by scalar relativistic norm conserving pseudo potentials with 16 and 6 valence electrons for Ce and O, while the valence electrons were described with an auxiliary plane wave basis set with a cutoff of 500 Ry and using the Gamma point for Brillouin-zone integration. The Ce-4f occupancies entering the Hubbard U term were calculated on the basis of Mulliken population analysis, while the value of the parameter U was set to 7.0 eV, which was determined in previous works.[10,35] It is worth noting that there was no ceria reduction nor any change in the occupation of the Ce-4f states during these simulations, and therefore the dynamics calculated with and without the inclusion of the Hubbard U term led to the same results. The canonical ensemble was employed with a target temperature of 350 K using the "canonical sampling velocity rescaling" thermostat proposed by Bussi and co-workers[36] and a time step of 0.5 fs. The AIMD simulations generated ∼30 ps of equilibrated trajectories (see Supplementary Note 3). The hydrogen atoms were described as deuterium atoms.

The Pt/CeO_2/water system was modeled by a Pt_6 cluster supported on a stoichiometric $CeO_2(111)$ surface. The lowest-energy morphology of the supported cluster was determined in a previous work.[37] The CeO_2 substrate was modeled with (4×4) supercell slabs consisting of three O−Ce−O trilayer and separated by more than 15 Å in the direction perpendicular to the surface. The lowest-laying atoms in the O−Ce−O trilayer were constrained to their equilibrium bulk-like positions, while all other atoms were free to move under the action of the interatomic forces. The space between the periodic ceria slabs was filled with 66 H_2O molecules. The MD simulations for this Pt_6/CeO_2 system, as well as for reduced ceria surfaces, were performed with the Quantum-ESPRESSO package[46] and employed a plane-waves basis set and ultrasoft pseudopotentials. We used the PBE+U method as implemented by Cococcioni and de Gironcoli[38] and, following our

DOI: 10.1021/jacs.6b03446
J. Am. Chem. Soc. 2016, 138, 11560−11567

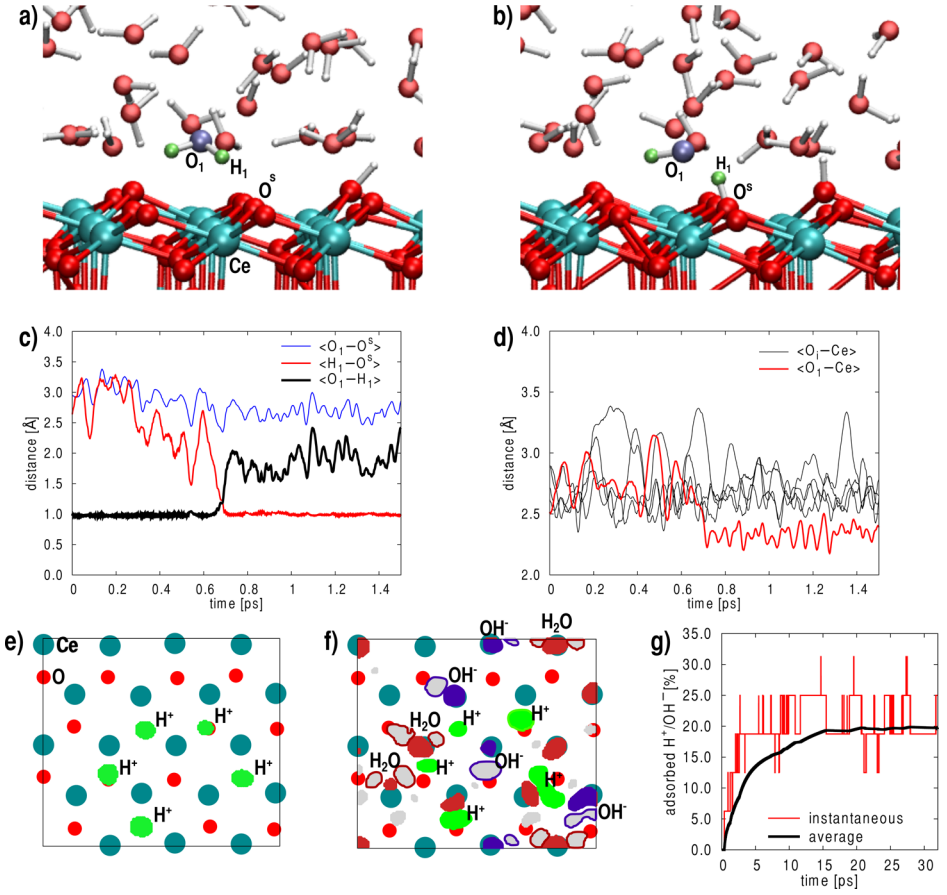

Figure 2. Representative AIMD configurations showing the initial (a) and final (b) states of water dissociation leading to a surface hydroxyl group and to a solvated hydroxide. (c,d) Time evolution of representative interatomic distances (denoted by "⟨ ⟩" symbols) during water dissociation. Surface O atoms are labeled by O^S, O_1, and H_1 refer to the O and H atoms involved in a specific water dissociation, while O_i indicates other water O atoms. (e,f) Spatial probability distribution function of O and H atoms averaged over planes at 1 Å (e) and 2.5 Å (f) from the CeO_2 surface. Number of adsorbed H^+/OH^- as a function of time (g). Light green, dark red, purple, and gray areas represent the distribution of the protons, water O atoms, hydroxide O atoms, and water/hydroxide H atoms, respectively. Criteria used to distinguish molecular and dissociated water molecules at surfaces are specified in the Supplementary Note 2.

previous works, set the value of the parameter U to 4.5 eV.[39−44] The plane-wave energy cut off limiting the basis set used to describe the electronic wave function and density were set to 25 and 250 Ry, respectively. Integrals in the Brillouin zone were performed at the Γ-point. The accuracy of these parameters in the MD simulations was determined and tested in our previous work (see Supporting Information in ref 45). The canonical ensemble was sampled with the Car−Parrinello propagation scheme, employing a fictitious orbital mass of 500 au and a time step of 0.12 fs, for a total of ∼30 ps of equilibrated trajectories. The target temperature of 350 K was controlled with a Nose−Hoover thermostat chain for ions and electrons. The hydrogen atoms were described as deuterium atoms. A second set of AIMD simulations (>30 ps) was run without the water layer so as to assess solvation effects.

Additional details on the computational set ups, on the reasons for using different PBE+U implementations (CP2K and QE), as well as on the comparison between these two approaches are included in the Supplementary Note 4.

RESULTS

Water Dissociation and Short-Range Proton Transfer.

In our DFT simulations, we initially focus on the interface between liquid water and the pure $CeO_2(111)$ surface (Figure 1a). Starting from a slab of thermally equilibrated liquid water having bulk structure (Figure 1a), the interaction with the oxide surface drives the barrierless dissociation of a fraction of the interfacial water molecules and quickly leads to partial surface hydroxylation. A representative snapshot of the equilibrated interface structure resulting from the AIMD simulations is displayed in Figure 1b. The analysis of the trajectories shows that the dissociation of the interfacial water molecules proceeds via proton transfer to the closest surface O atoms. This leads to the formation of surface hydroxy groups and of solvated hydroxide ions (green and violet atoms in Figure 1b), which increase the solvent density at the interface (Figure 1c). One instance of this elementary reaction is displayed in Figure 2a,b.

We analyze this proton transfer reaction in Figure 2c, by plotting the time evolution of the interatomic distances between the surface O^S and water O_1, H_1 atoms. The resulting hydroxide ion interacts with the surface Ce^{4+} sites more strongly than the neutral water molecules, hence hydroxides do not diffuse in the liquid bulk as they are confined at the interface by electrostatics. This increased interaction is reflected in the ∼15% shortening of the $\langle O_1{-}Ce\rangle$ distance after dissociation (Figure 2d). The spatial probability distribution function averaged over planes at 1 and 2.5 Å from the surface shows that, at equilibrium, the hydroxide ions reside indeed on the surface Ce^{4+} sites, while the remaining cation sites coordinate a solvent water molecule (Figure 2e,f). This analysis also shows that the surface cation sublattice acts as a template

DOI: 10.1021/jacs.6b03446
J. Am. Chem. Soc. 2016, 138, 11560−11567

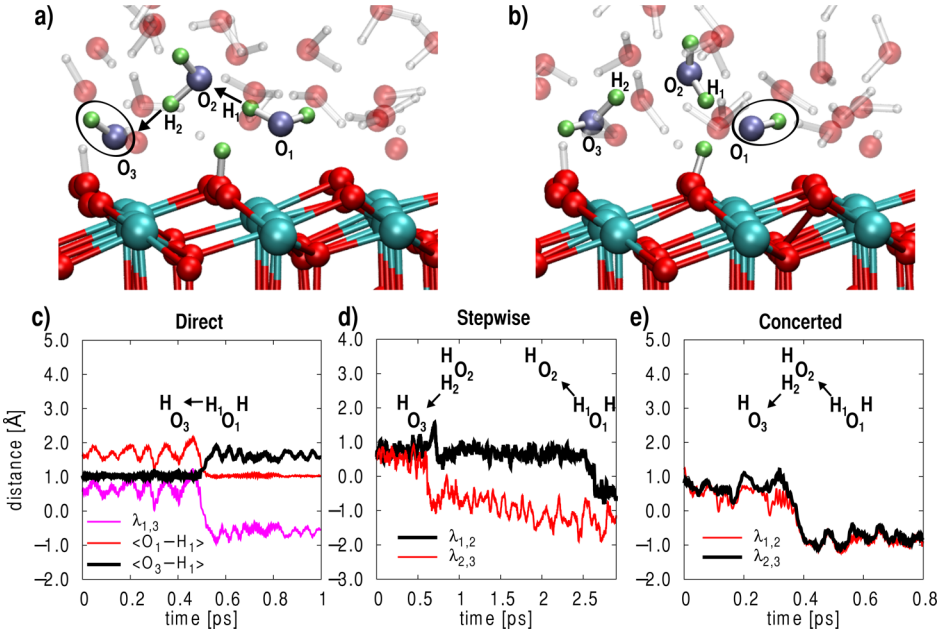

Figure 3. Representative AIMD configurations showing the initial (a) and final (b) states of the proton chain leading to long-range hydroxide diffusion at the ceria/water interface. (c–e) Time evolution of representative interatomic distances (denoted by "⟨ ⟩") and collective variables during hydroxide diffusion. See text and Figure 4d for definition of λ.

for the water/hydroxide ad-species, transferring its symmetric atomic arrangement to the first surface solvation layer, which is therefore highly structured. As a result, the equilibrium water coverage at the oxide surface is close to 1 ML, and corresponds to a 60% increase of the water density at the solid/liquid interface, with a density peak of 1.65 g/cm^3 at ∼2 Å from the oxide surface (Figure 1c).

The statistics of water dissociation accumulated during the simulations (Figure 2g) show that equilibrium is reached after ∼15 ps, in which an average of ∼20% of the surface O sites (denoted as O^S) are hydroxylated. As a result, Ce−O^SH^+, Ce−OH^-, and Ce−OH_2 sites coexist on the solvated surface, which therefore displays amphoteric behavior.[47] Similarly to what reported for other oxide surfaces,[9−11] after this transient, the dissociation of water molecules in the first surface solvation layer becomes a reversible dynamic process, which is governed by solvent-induced short-ranged transfers of protons between adsorbed water (Ce−OH_2) and the surface O^S sites, or, in the reverse process, between surface hydroxy groups (Ce−O^SH^+) and hydroxide ions (Ce−OH^-). Our results demonstrate that the solvent-induced proton hopping identified by Tocci and Michaelides for the ZnO(10$\bar{1}$0) non-reducible surface[9] is also active at the CeO_2(111) highly reducible surface.

We remark that during all the MD simulations reported above, the water interaction and dissociation at the stoichiometric CeO_2(111) surface does not induce substrate reduction; i.e., all the Ce ions preserve their 4+ oxidation state (Supplementary Figure 7). Instead, repeating the simulations starting from a reduced ceria surface, i.e., including an O vacancy and the related two Ce^{3+} ions in the ceria slab, we observe that one interfacial water molecule quickly (∼70 fs) dissociates at the O vacancy, leading to the formation of two surface hydroxy Ce−O^SH^+ groups (Supplementary Figure 8) and two substrate Ce^{3+} ions, in full analogy to the vacuum case.[27−29]

Hydroxide Dynamics and Long-Range Proton Transfer. Besides the short-range proton transfer, the analysis of the AIMD trajectories reveals the existence of another diffusion process active at the water/oxide interface. This is a longer ranged proton transfer that determines the diffusion of protons and hydroxide ions along the solid−liquid interface (Figure 3), effectively leading to hydroxide hopping between surface sites separated by more than 3.5 Å. To analyze this more complex process, we introduce two collective variables (CVs): $d_{i,j} = O_i - O_j$ and $\lambda_{i,j} = \langle O_i - H_i \rangle - \langle O_j - H_i \rangle$, where i and j label water or hydroxide molecules in the simulation cell.[48] The time evolution of some of these CVs during three representative proton-transfer events is displayed in Figure 3, while their physical meaning is graphically represented in Figure 4e. $d_{i,j}$ is the distance between the two O atoms of water/hydroxide molecules labeled by i and j (see black dashed lines in Figure 4e). $\lambda_{i,j}$ describes the position of a proton with respect to the O atoms of the two water molecules i and j (red dotted lines in Figure 4e): when $\lambda_{i,j} > 0$ the proton is bound to O_j, while when $\lambda_{i,j} < 0$ the proton is bound to O_i.

By analyzing the trajectories with these CVs, we identify two active mechanisms for interface hydroxide diffusion: (i) A direct proton transfer between an adsorbed water molecule and a neighboring hydroxide ion (Figure 3c), and (ii) proton transfer chains mediated by solvent water molecules, which bridge between surface hydroxide and surface water molecules (stepwise, Figure 3 d, or concerted, Figure 3e). In the latter case, the mechanism involves two proton transfers: One proton transfers from the assisting water molecule (H_2 in Figure 3) to the hydroxide (O_3−H), hence transforming it into an interfacial water molecule. The other proton transfers from the adsorbed (H_1) to the assisting water molecule, hence transforming the former into a surface hydroxide. The overall effect of this diffusion process, which is reminiscent of the Grotthus mechanism between Zundel and Eigen complexes in bulk water,[49] is to transfer hydroxide ions selectively along the water/oxide interface between different surface sites.

Thermodynamics and Kinetics. We calculate the free energy ΔG controlling these short- and long-range proton

DOI: 10.1021/jacs.6b03446
J. Am. Chem. Soc. 2016, 138, 11560−11567

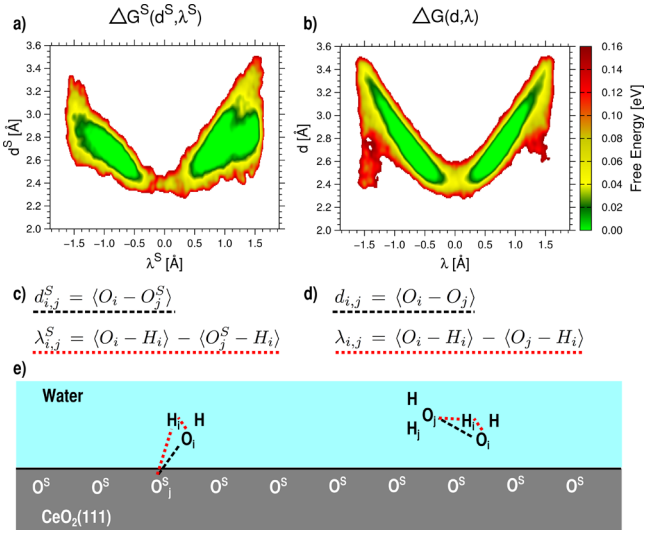

Figure 4. Calculated free energy maps for the short-range proton transfer (a) and long-range hydroxide diffusion (b) as a function of the corresponding collective variables defined in panels (c) and (d). (e) Scheme indicating the interatomic distances entering the definition of d^S and d (see black dashed lines), and of λ^S and λ (see red dotted lines).

transfers at T = 350 K by applying the formula $\Delta G = -k_B T \log P$, where k_B is the Boltzmann constant and P is the probability distribution function defined in terms of CVs capturing the different diffusion mechanisms. For the long-range process, the probability function P is obtained from the AIMD trajectories by accumulating the population histograms of the $d_{i,j}$ and $\lambda_{i,j}$ variables introduced above:

$$P(d, \lambda) = \int_0^\infty \sum_{i \neq j} \delta(d - d_{i,j}(t))\delta(\lambda - \lambda_{i,j}(t))\mathrm{d}t$$

where δ is the Dirac function. The probability function for the short-range process P^S is obtained with an equivalent methodology employing the modified CVs $d^S_{i,j} = \langle O_i - O^S_j \rangle$ and $\lambda^S_{i,j} = \langle O_i - H_i \rangle - \langle O^S_j - H_i \rangle$, where the index i labels the water/hydroxide molecules, while j labels the surface oxygen atoms, O^S (Figure 4e). $d_{i,j}$ is the distance between a surface O^S atom and a water O atom, labeled by j and i, respectively. It therefore captures whether surface proximity of the water molecule is relevant for its dissociation and for proton transfer to the surface. $\lambda^S_{i,j}$ describes the position of the proton, whether bound to the surface ($\lambda^S_{i,j} > 0$) or to a water molecule ($\lambda^S_{i,j} < 0$) The resulting free energy maps are displayed in Figure 4, while the corresponding probability distribution functions (P, P^S) are reported in Supplementary Figure 1.

Figure 4 plots the free energy differences for the short- and long-range proton transfers, ΔG^S and ΔG respectively, calculated in the two-dimensional subspace spanned by the corresponding CVs. The green areas in Figure 4a represent the distinct free energy basins in which a proton is bound to the surface (O^S–H state, right) or to a water molecule (H–O–H state, left). The free energy map is asymmetric because the two minima refer to chemically different configurations, which therefore undergo different equilibrium dynamics. In particular, the system in the O^S–H surface state explores a larger range of interatomic distances. Consequently, the forward and backward reactions are also different, being related to water dissociation or formation. From this analysis we estimate the activation energy for the short-range proton diffusion to be ~0.1 eV, which is in line with the values calculated by Tocci and Michaelideas for the same process on wet ZnO surfaces.[9]

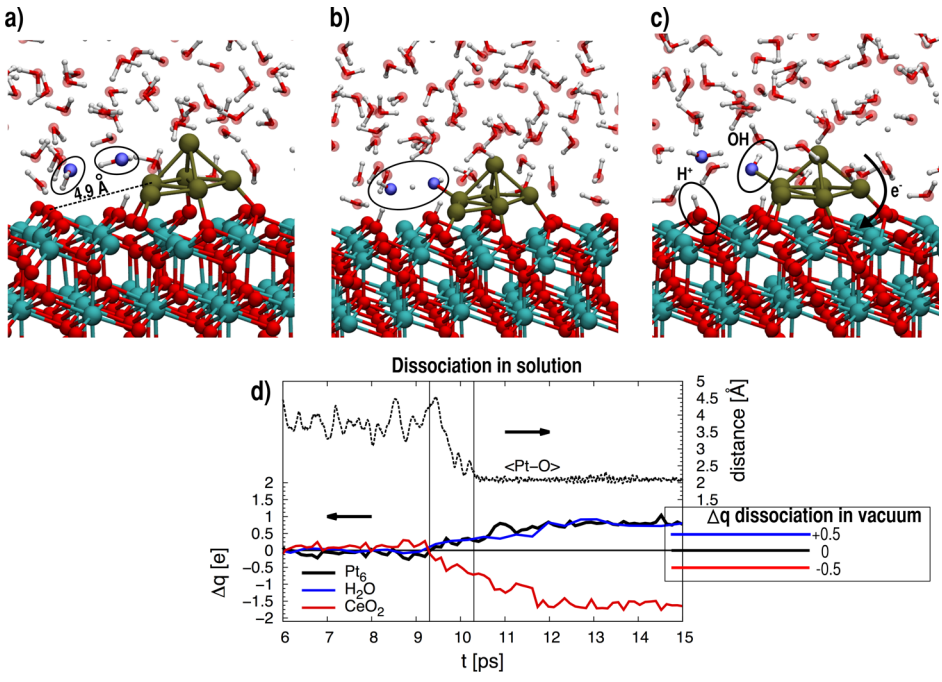

Figure 5. Snapshots from the AIMD simulations showing the initial (a), intermediate (b), and final (c) configurations for water dissociation at the periphery of a Pt_6 cluster supported by the CeO_2 surface. (d) Analysis of the reaction in terms of the ⟨Pt–O⟩ distance (dashed line) and of the charge difference (Bader) calculated for the Pt_6 cluster, H_2O molecules, and CeO_2 slab (solid lines). Negative/positive values of Δq indicate electron increase/decrease. The inset in panel (d) reports the charge difference analysis for water dissociation in vacuum.

DOI: 10.1021/jacs.6b03446
J. Am. Chem. Soc. 2016, 138, 11560–11567

The free energy map for the long-range proton transfer is displayed in Figure 4b. It is obviously symmetric because the two minima refer to chemically equivalent configurations and because the interface is homogeneous and there is no preferential surface site for the hydroxide adsorption. Therefore, the forward and backward reactions are equivalent. The calculated activation energy for this process (0.07 eV) is as small as that one for interfacial water dissociation.

It is evident from the free energy maps in Figure 5 that water dissociation and proton diffusion are correlated with the shortening of O−O distances (d^S and d CVs). The increased water density at the ceria/water interface shortens the O−O distance and therefore promotes the fast interface diffusion processes.

Relevance for Wet Catalysis: Ceria-Supported Pt Clusters. The small activation energy for long-range hydroxide diffusion along the water/ceria interface indicates that this process could participate in the wet heterogeneous catalysis of ceria-based materials at room temperature. To demonstrate this, we focus on a Pt_6 nanoparticle supported by the $CeO_2(111)$ surface. Ceria-supported Pt nanoparticles are key catalysts in fuel production and purification, environmental chemistry, and chemical industry.[20] To assess the relevance of the long-range proton transfer on the catalysis of supported Pt nanoparticles, we consider the $Pt_6/CeO_2(111)$ model system, which we have fully characterized in the gas phase.[37]

We show here specific instances in which the interface diffusion mechanisms described above participate into the water dissociation catalyzed by the Pt nanoparticles, accelerating the direct spillover of the H/OH species over distances larger than 4.9 Å. Three snapshots from the AIMD simulation representing this event occurring during the AIMD simulation run are displayed in Figure 5a−c.

A water molecule of the solvation layer dissociates at the periphery of the supported nanoparticle into a hydroxide ion and a proton. This activates the dissociation of a neighboring solvent water molecule (see ovals in Figure 5a,b), which mediates the fast proton chains at the water/oxide interface described before and effectively transfers the proton at an oxide surface site 4.9 Å away from the nanoparticle, forming a surface hydroxyl (Figure 5c). The resulting OH^- species readily binds to a Pt site of the supported cluster where it drives substantial charge transfer across the metal/oxide interface.

The electron reorganization of the Pt/CeO_2 nanocatalyst is analyzed in Figure 5d in terms of Bader charge differences (Δq) calculated for the Pt_6, water, and CeO_2 slabs (solid lines), and of the Pt−OH distance (dashed line). This plot reveals two concomitant charge transfers driven by water dissociation at the solvated Pt/ceria interface (see the region between the vertical lines): (i) The cluster transfers one electron to the ceria substrate (black line), and (ii) the hydroxide ion binds to the Pt cluster and releases one electron, thus turning into a neutral OH adsorbate (blue line). Quite surprisingly, the latter electron is also transferred to the ceria substrate. Overall, about two electrons, one from the hydroxide species and one from the cluster, are transferred from the OH-Pt_6 system to the oxide substrate through the metal/oxide interface (red line), thus demonstrating that the cluster/solvent and metal/oxide interfaces are strongly coupled. The reason for this effect stems from the high reducibility of the substrate, which can accommodate the excess electrons on the Ce-f states by the easy $Ce^{4+} \rightarrow Ce^{3+}$ oxidation changes.

By comparing the simulations of the Pt/CeO_2 surface in vacuum and in solution, we can anticipate that the solvent increases the charge transfer from the cluster to the ceria support by ∼1−2 electrons, so that, on average, the charge of the cluster decreases upon solvation. However, it turns out that the solvation effects on the electronic properties of the catalyst and on the charge state of the supported nanoparticle are complex and dependent on many factors, including the adsorption and dissociation sites of the water molecules, the relative distance between the dissociated H and OH products adsorbed on the catalyst, the dynamic evolution of the cluster structure, and others. Due to this complexity, a complete analysis of these effects will be reported elsewhere,[50] while we focus here primarily on the catalytic effects of proton diffusion at (Pt)ceria/water interface. Our vacuum simulations for water dissociation at the Pt_6/CeO_2 catalysis never showed the two-electron charge transfer reported above for the solvated catalyst. The charge analysis of the initial and final states of water dissociation is displayed in the inset of Figure 5d. It shows that the vacuum reaction environment reduces the charge transfer by a factor of ∼2. Most importantly, in vacuum, the charge transferred involves only the hydroxide adsorbate and the ceria surface, while the cluster charge remains unaffected.

We note that, given the concerted reaction mechanism, the process described above cannot be distinguished from the one in which a water molecule dissociates at a ceria surface site far from the cluster and the hydroxide ion is then transferred to the Pt nanoparticle by the proton chain in the solvent (Figure 5 c-b-a sequence). In both cases, the supported Pt clusters acts as a basin of attraction for the hydroxide products, which therefore will accumulate at the cluster sites.

DISCUSSION

The molecular and dissociative adsorption of water on $CeO_2(111)$ in vacuum conditions and at T = 0 K were reported to be almost isoenergetic and to be separated by a small energy barrier (<0.2 eV).[26,29] Quite consistently, our simulations demonstrate that room temperature wet reaction conditions drive the spontaneous dissociation of a fraction of the interfacial water molecules. The dissociated state is further stabilized by hydroxide solvation and electrostatic screening by the solvent. The spontaneous dissociation of interfacial water molecules indicates that the O sites of the clean $CeO_2(111)$ surface act as Brønsted bases. The resulting partial hydroxylation of the solvated ceria surface generates two interface-specific sites, Ce−OH_2 and Ce−OH^-, that form a conjugate pair and that govern the proton hopping along the ceria/water interface reported above. In this framework, the proton chains leading to the hydroxyl diffusion proceed between the Ce−OH_2 and Ce−OH^- sites, which act as Brønsted acid and base, respectively. The water-ceria interface therefore has a clear amphoteric behavior, in line with other oxides such as SiO_2, TiO_2 or ZrO_2.[8,51,52] Similar conjugate pairs involving sites of the oxide and of the supported Pt nanoparticle determine the accelerated spillover of ad-species between the metal and oxide sites during wet catalysis. On the basis of these results we cannot address the issue of competitive adsorption on solvated surface catalysts. In the context of Mars and Van Krevelen mechanisms at oxide-supported metal catalysts, the proton transfer at the metal−support interface has been shown to be a key reaction step in several reactions, promoting the binding and selected activation of adsorbed intermediates.[58,59] The amphoteric nature of the Pt/CeO_2 surface certainly plays an

DOI: 10.1021/jacs.6b03446
J. Am. Chem. Soc. 2016, 138, 11560−11567

important role in these cases: The same basic sites that accept a proton and form solvated hydroxy species can in a later stage become acid sites and transfer the proton to the supported metal, thus participating into complex catalytic reactions.

The point of zero net proton charge (PZC) measured for ceria systems are typically above 7: In particular, Trasatti and co-workers reported a PZC value of 8.1 for several commercial samples.[53,54] The present calculations are a valuable starting point for a theoretical prediction of the PZC; however, its reliable calculation requires more specific approaches capable to address the acidities of the related surface groups, such as those developed and applied for TiO_2 or SiO_2 surfaces.[51,52] In this context, we note that, by construction, our simulations sample the PZC surface condition, since the concentrations of the surface Ce−OH^+ hydroxy and the Ce−OH^- hydroxylates turn out to be equal, both of them resulting from the dissociation of neutral water molecules.

Our results for the solvated Pt/CeO_2 system demonstrate how solvation of oxide-supported metal nanocatalysts can strongly modify the electronic structure of the catalyst, affecting the metal−support interaction, which is central for the increased catalytic activity displayed by metal clusters supported on reducible oxides.[21−23] In particular, it is well established that the higher activity of Pt/ceria catalysts as compared to pure Pt systems stems from the O-storage capacity and high reducibility of the ceria support,[20] which activate the supported Pt particles via electron transfer at the metal/oxide interface and via strong metal−support interaction. To date, the majority of the theoretical studies addressing the interaction between ceria and water were static calculations performed at T = 0 K and focused on the adsorption of a single or few water molecules on clean or reduced CeO_2 surfaces.[26−29] Previous AIMD simulations of ceria surfaces in vacuum conditions indeed established the importance of dynamic processes at ceria-based catalytic surfaces.[10,41] The present results demonstrate how the rich dynamics of the solid/liquid interface impact on the metal−support interaction and hence on the catalytic properties of oxide-supported metal nanoparticles in wet conditions.

CONCLUSIONS

Our simulations show that, upon solvation, surfaces of ceria-based materials can become proton conductors. Similar conclusions were reported for bohemite surface steps and for hydrated zirconia (ZrO_2) surfaces.[19,8] Indeed, high conductivity has been measured for nanostructured ceria and zirconia materials in humidified atmosphere.[55] It was proposed that the origin of this high conductivity is related to the presence of water layers trapped between the grain boundaries of the polycrystalline materials.[56] The present theoretical results provide atomic-level support to the low-T proton conductivity of ceria-based systems and therefore underpin their possible application as electrolytes in fuel cells.[57] More generally, the accelerated spillover between metal and oxide sites, together with its impact on the metal−support interaction, opens new perspectives in wet heterogeneous catalysis by oxide-supported metal nanoparticles.

ASSOCIATED CONTENT

Supporting Information

The Supporting Information is available free of charge on the ACS Publications website at DOI: 10.1021/jacs.6b03446.

Supplementary Note 1, probability distributions and free energies; Supplementary Note 2, criteria for defining the number of adsorbed H^+/OH^- groups; Supplementary Note 3, further details of the slab model used to simulate water/ceria interfaces; Supplementary Note 4, further computational details and validation of the computational parameters; Supplementary Note 5, XYZ coordinates; Supplementary Figures 1−8 (PDF)

AUTHOR INFORMATION

Corresponding Authors

*mfarnesi@sissa.it

*fabris@democritos.it

Present Address

‖F.N.R.: Universidade Federal do ABC, Av. dos Estados, 5001 Bairro Bangu, Santo André SP, CEP 09210-580 Brazil

Notes

The authors declare no competing financial interest.

ACKNOWLEDGMENTS

This work was supported by the European Union via the FP7-NMP-2012 project chipCAT under Contract No. 310191 and the EU FP7 COST action CM1104. S.F. acknowledges the support provided by the Humboldt Foundation through a Friedrich Wilhelm Bessel Research Award. The simulations were carried out on the supercomputers in NIMS, The University of Tokyo, and the Kyushu University through the HPCI System Research Projects (Project IDs: hp150055, hp150068, hp160040, hp160080) as well as on the CINECA through the ISCRA initiative. This work was supported in part by JSPS and MEXT KAKENHI Grant Numbers JP15K05138 and JP15H05701.

REFERENCES

(1) Corma, A.; Garcia, H. *Chem. Soc. Rev.* **2008**, *37*, 2096−2126.

(2) Date, M.; Okumura, M.; Tsubota, S.; Haruta, M. *Angew. Chem., Int. Ed.* **2004**, *43*, 2129−2132.

(3) Monai, M.; Montini, T.; Chen, C.; Fonda, E.; Gorte, R. J.; Fornasiero, P. *ChemCatChem* **2015**, *7*, 2038−2046.

(4) Cheng, J.; Liu, X.; Kattirtzi, J. A.; VandeVondele, J.; Sprik, M. *Angew. Chem., Int. Ed.* **2014**, *53*, 12046−12050.

(5) Brown, G. E., Jr.; Henrich, V. E.; Casey, W. H.; Clark, D. L.; Eggleston, C.; Felmy, A.; Goodman, D. W.; Gratzel, M.; Maciel, G.; McCarthy, M. I.; Nealson, K. H.; Sverjensky, D. A.; Toney, M. F.; Zachara, J. M. *Chem. Rev.* **1999**, *99*, 77−174.

(6) Merte, L. R.; Peng, G.; Bechstein, R.; Rieboldt, F.; Farberow, C. A.; Grabow, L. C.; Kudernatsch, W.; Wendt, S.; Lægsgaard, E.; Mavrikakis, M.; Besenbacher, F. *Science* **2012**, *336*, 889−893.

(7) Merte, L. R.; Bechstein, R.; Peng, G.; Rieboldt, F.; Farberow, C. A.; Zeuthen, H.; Knudsen, J.; Lægsgaard, E.; Wendt, S.; Mavrikakis, M.; Besenbacher, F. *Nat. Commun.* **2014**, *5*, 4193.

(8) Sato, R.; Ohkuma, S.; Shibuta, Y.; Shimojo, F.; Yamaguchi, Y. *J. Phys. Chem. C* **2015**, *119*, 28925−28933.

(9) Tocci, G.; Michaelides, A. *J. Phys. Chem. Lett.* **2014**, *5*, 474−480.

(10) Wang, Y.-G.; Mei, D.; Glezakou, V.-A.; Li, J.; Rousseau, R. *Nat. Commun.* **2015**, *6*, 6511.

(11) Akimov, A. V.; Muckerman, J. T.; Prezhdo, O. V. *J. Am. Chem. Soc.* **2013**, *135*, 8682−8691.

(12) Farnesi Camellone, M.; Marx, D. J. *J. Phys. Chem. Lett.* **2013**, *4*, 514−518.

(13) Ping, Y.; Goddard, W. A., III; Galli, G. A. *J. Am. Chem. Soc.* **2015**, *137*, 5264−5267.

(14) Nirmalraj, P.; Thompson, D.; Molina-Ontoria, A.; Sousa, M.; Martín, N.; Gotsmann, B.; Riel, H. *Nat. Mater.* **2014**, *13*, 947−953.

(15) Andanson, J.-M.; Baiker, A. *Chem. Soc. Rev.* **2010**, *39*, 4571−4584.
(16) Carrasco, J.; Hodgson, A.; Michaelides, A. *Nat. Mater.* **2012**, *11*, 667−674.
(17) Hass, K. C.; Schneider, W. F.; Curioni, A.; Andreoni, W. *Science* **1998**, *282*, 265−268.
(18) Sulpizi, M.; Gaigeot, M. P.; Sprik, M. *J. Chem. Theory Comput.* **2012**, *8*, 1037−1047.
(19) Motta, A.; Gaigeot, M.-P.; Costa, D. *J. Phys. Chem. C* **2012**, *116*, 12514−12524.
(20) Trovarelli, A. *Catalysis by ceria and related materials; Catalytic Science Series*; Imperial College Press: London, 2002.
(21) Campbell, C. T. *Nat. Chem.* **2012**, *4*, 597−598.
(22) Bruix, A.; Rodriguez, J. A.; Ramírez, P. J.; Senanayake, S. D.; Evans, J.; Park, J. B.; Stacchiola, D.; Liu, P.; Hrbek, J.; Illas, F. *J. Am. Chem. Soc.* **2012**, *134*, 8968−8974.
(23) Lykhach, Y.; Kozlov, S. M.; Skála, T.; Tovt, A.; Stetsovych, V.; Tsud, N.; Dvořák, F.; Johánek, V.; Neitzel, A.; Mysliveček, J.; Fabris, S.; Matolín, V.; Neyman, K. M.; Libuda, J. *Nat. Mater.* **2016**, *15*, 284−288.
(24) Mullins, D. R.; Albrecht, P. M.; Chen, T.-L.; Calaza, F. C.; Biegalski, M. D.; Christen, H. M.; Overbury, S. H. *J. Phys. Chem. C* **2012**, *116*, 19419−19428.
(25) Vayssilov, G. N.; Lykhach, Y.; Migani, A.; Staudt, T.; Petrova, G. P.; Tsud, N.; Skála, T.; Bruix, A.; Illas, F.; Prince, K. C.; Matolín, V.; Neyman, K. M.; Libuda, J. *Nat. Mater.* **2011**, *10*, 310−315.
(26) Fernandez-Torre, D.; Kosmider, K.; Carrasco, J.; Ganduglia-Pirovano, M. V.; Perez, R. *J. Phys. Chem. C* **2012**, *116*, 13584−13593.
(27) Hansen, H. A.; Wolverton, C. *J. Phys. Chem. C* **2014**, *118*, 27402−27414.
(28) Marrocchelli, M.; Yildiz, B. J. *J. Phys. Chem. C* **2012**, *116*, 2411−2424.
(29) Szabová, L.; Tateyama, Y.; Matolín, V.; Fabris, S. *J. Phys. Chem. C* **2015**, *119*, 2537−2544.
(30) Perdew, J. P. J.; Burke, K.; Ernzerhof, M. *Phys. Rev. Lett.* **1996**, *77*, 3865−3868.
(31) Da Silva, J. L. F.; Ganduglia-Pirovano, M. V.; Sauer, J.; Bayer, V.; Kresse, G. *Phys. Rev. B: Condens. Matter Mater. Phys.* **2007**, *75*, 045121.
(32) Loschen, C.; Carrasco, J.; Neyman, K. M.; Illas, F. *Phys. Rev. B: Condens. Matter Mater. Phys.* **2007**, *75*, 035115.
(33) Paier, J.; Penschke, C.; Sauer, J. *Chem. Rev.* **2013**, *113*, 3949−3985.
(34) VandeVondele, J.; Krack, M.; Mohamed, F.; Parrinello, M.; Chassaing, T.; Hutter, J. *Comput. Phys. Commun.* **2005**, *167*, 103−128.
(35) Wang, Y. G.; Mei, D.; Li, J.; Rousseau, R. *J. Phys. Chem. C* **2013**, *117*, 23082−23089.
(36) Bussi, G.; Donadio, D.; Parrinello, M. *J. Chem. Phys.* **2007**, *126*, 014101.
(37) Ribeiro Negreiros, F.; Fabris, S. *J. Phys. Chem. C* **2014**, *118*, 21014−21020.
(38) Cococcioni, M.; de Gironcoli, S. *Phys. Rev. B: Condens. Matter Mater. Phys.* **2005**, *71*, 035105.
(39) Fabris, S.; Vicario, G.; Balducci, G.; De Gironcoli, S.; Baroni, S. *J. Phys. Chem. B* **2005**, *109*, 22860−22867.
(40) Fabris, S.; de Gironcoli, S.; Baroni, S.; Vicario, G.; Balducci, G. *Phys. Rev. B: Condens. Matter Mater. Phys.* **2005**, *71*, 041102.
(41) Camellone, M. F.; Fabris, S. *J. Am. Chem. Soc.* **2009**, *131*, 10473−83.
(42) Szabová, L.; Camellone, M. F.; Huang, M.; Matolín, V.; Fabris, S. *J. Chem. Phys.* **2010**, *133*, 234705.
(43) Ghosh, P.; Farnesi Camellone, M.; Fabris, S. *J. Phys. Chem. Lett.* **2013**, *4*, 2256−2263.
(44) Dvorak, F.; Farnesi Camellone, M.; Tovt, A.; Tran, N.-D.; Negreiros, F. R.; Vorokhta, M.; Skala, T.; Matolinova, I.; Myslivecek, J.; Matolın, V.; Fabris, S. *Nat. Commun.* **2016**, *7*, 10801.
(45) Ribeiro Negreiros, F.; Farnesi Camellone, M.; Fabris, S. *J. Phys. Chem. C* **2015**, *119*, 21567−21573.
(46) Giannozzi, P.; et al. *J. Phys.: Condens. Matter* **2009**, *21*, 395502.
(47) The $-O^S$ and Ce− notation is used to represent the O and Ce surface sites of the $CeO_2(111)$ surface.
(48) We drop here the additional label necessary to differentiate between the two H atoms in a given water molecule *i*.
(49) Grotthuss, T. *Ann. Chim.* **1806**, *58*, 54−73.
(50) Szabova, L.; Farnesi Camellone, M.; Tateyama, T.; Fabris, S., manuscript in preparation.
(51) Cheng, J.; Sprik, M. *J. Chem. Theory Comput.* **2010**, *6*, 880−889.
(52) Sulpizi, M.; Gaigeot, M. P.; Sprik, M. *J. Chem. Theory Comput.* **2012**, *8*, 1037−1047.
(53) De Faria, L. A.; Trasatti, S. *J. Colloid Interface Sci.* **1994**, *167*, 352−357.
(54) Kosmulski, M. *Adv. Colloid Interface Sci.* **2009**, *152*, 14−25.
(55) Takamura, H.; Takahashi, N. *Solid State Ionics* **2010**, *181*, 100−103.
(56) Miyoshi, S.; Akao, Y.; Kuwata, N.; Kawamura, J.; Oyama, Y.; Yagi, T.; Yamaguchi, S. *Chem. Mater.* **2014**, *26*, 5194−5200.
(57) Kim, S.; Anselmi-Tamburini, U.; Park, H. J.; Martin, M.; Munir, Z. A. *Adv. Mater.* **2008**, *20*, 556−559.
(58) Saavedra, J.; Doan, H. A.; Pursell, C. J.; Grabow, L. C.; Chandler, B. D. *Science* **2014**, *345*, 1599−1602.
(59) Nelson, R. C.; Baek, B.; Ruiz, P.; Goundie, B.; Brooks, A.; Wheeler, M. C.; Frederick, B. G.; Grabow, L. C.; Austin, R. N. *ACS Catal.* **2015**, *5*, 6509−6523.

DOI: 10.1021/jacs.6b03446
J. Am. Chem. Soc. 2016, 138, 11560−11567